

Measurement of Spin–Orbit Alignment in an Extrasolar Planetary System

Joshua N. Winn^{1,2}, Robert W. Noyes¹, Matthew J. Holman¹, David Charbonneau¹,
Yasuhiro Ohta³, Atsushi Taruya^{3,4}, Yasushi Suto^{3,4}, Norio Narita³, Edwin L. Turner^{3,5},
John A. Johnson⁶, Geoffrey W. Marcy⁶, R. Paul Butler⁷, Steven S. Vogt⁸

ABSTRACT

We determine the stellar, planetary, and orbital properties of the transiting planetary system HD 209458, through a joint analysis of high-precision radial velocities, photometry, and timing of the secondary eclipse. Of primary interest is the strong detection of the Rossiter-McLaughlin effect, the alteration of photospheric line profiles that occurs because the planet occults part of the rotating surface of the star. We develop a new technique for modeling this effect, and use it to determine the inclination of the planetary orbit relative to the apparent stellar equator ($\lambda = -4.4 \pm 1.4$), and the line-of-sight rotation speed of the star ($v \sin I_\star = 4.70 \pm 0.16 \text{ km s}^{-1}$). The uncertainty in these quantities has been reduced by an order of magnitude relative to the pioneering measurements by Queloz and collaborators. The small but nonzero misalignment is probably a relic of the planet formation epoch, because the expected timescale for tidal coplanarization is larger than the age of the star. Our determination of $v \sin I_\star$ is a rare case in which rotational line broadening has been isolated from other broadening mechanisms.

Subject headings: stars: individual (HD 209458)—stars: rotation—planetary systems: formation

1. Introduction

A star and its planets inherit their angular momentum from a common source: the rotation of the molecular cloud from which they formed. It follows that the axes of planetary orbits should be closely aligned with the rotation axis of the star, an expectation that is fulfilled in the solar system. The rotation axis of the Sun is tilted by only 6° relative to the axis defined by the net angular momentum of the planetary orbits (see Beck & Giles 2005, and references therein). Indeed, the observed coplanarity of solar system

¹Harvard-Smithsonian Center for Astrophysics, 60 Garden Street, Mail Stop 51, Cambridge, MA 02138

²Hubble Fellow

³Department of Physics, The University of Tokyo, Tokyo, 113-0033, Japan

⁴Research Center for the Early Universe, School of Science, The University of Tokyo, Tokyo 113-0033, Japan

⁵Princeton University Observatory, Peyton Hall, Princeton, NJ 08544

⁶Department of Astronomy, University of California, Mail Code 3411, Berkeley, CA 94720

⁷Department of Terrestrial Magnetism, Carnegie Institution of Washington, 5241 Broad Branch Road NW, Washington, DC 20015

⁸UCO/Lick Observatory, University of California, Santa Cruz, CA 95064

orbits was the main inspiration for Kant (1755) and Laplace (1796), who proposed that the Sun and its planets condensed from a spinning, flattened nebula.

It would be interesting to know whether this degree of alignment is typical of all planetary systems, or whether the solar system is anomalously well-aligned or misaligned. The degree of alignment depends on both poorly understood initial conditions and poorly understood physical processes. For example, the angular momentum distribution of the parent molecular cloud is surely inhomogeneous at some level. The star forms earlier than the planets, and might consequently be composed of material with a different net angular momentum than the material that falls in later. The star’s axis of rotation may be altered during the T Tauri phase, when much of its angular momentum is lost through bipolar outflows and magnetic coupling to the protoplanetary disk. There may be angular momentum evolution in the orbits during planetary migration, or as a consequence of gravitational interactions between protoplanets. The orbits may be altered by tidal interactions with the parent star, or torques from a companion star. It is even conceivable that there are planetary systems for which the orbital axes are grossly misaligned with the stellar rotation axis, due to a close encounter with another star, or the outright capture of planets from another star. The discovery of even a single example of such a system would be of interest. Thus, it would be desirable to have additional cases besides the solar system for which the degree of spin-orbit alignment can be assessed.

Furthermore, if it could be established that planetary orbits are universally well-aligned with the equatorial planes of their parent stars, there would be useful corollaries for some planet detection and characterization schemes, as reviewed by Hale (1994). For instance, the Doppler method does not reveal the mass M_p of the planet, but rather $M_p \sin I$, where I is the inclination of the orbit relative to the sky plane. It would be helpful if the inclination of the stellar rotation axis I_\star could be safely assumed to equal I , because then the various methods of estimating I_\star (through estimates of rotation periods, line broadening, and stellar radius) could be brought to bear on the problem. Indeed, some investigators have already found it convenient to assume $I = I_\star$ in interpreting radial velocity data (e.g., Hale 1995, Francois et al. 1996, Baliunas et al. 1997, Gonzalez 1998). Likewise, if $I = I_\star$, then stars that are viewed pole-on ($I_\star \approx 0^\circ$) would be good targets for direct-detection experiments, since the planets would always be viewed near maximum elongation.

For transiting planets, there is a powerful method available to measure spin-orbit alignment. The idea is to exploit a spectroscopic effect that was first described by Rossiter (1924) and McLaughlin (1924) for the case of eclipsing binary stars. During a transit, the planet occults a spot on the rotating surface of the star. The occultation thereby removes a particular velocity component from the rotationally broadened profiles of the stellar absorption lines. In principle, through observation of this missing velocity component, one can measure the line-of-sight velocity of the stellar disk ($v \sin I_\star$) at each point along the chord traversed by the planet, as well as the angle (λ) between the sky-projected angular momentum vectors of the planetary orbit and the stellar spin.

In practice, the spectral distortion produced by the Rossiter-McLaughlin (RM) effect is difficult to discern in a single spectral line. However, when the entire spectrum is analyzed, the RM effect manifests itself as an anomalous radial velocity. By “anomalous,” we mean an apparent wavelength shift of the spectral lines that differs from the Doppler shift caused by the star’s orbital motion. If the planet blocks a small portion of the blue wing of the line, then the line will appear to be slightly redshifted, and vice versa. Calculations of this effect were carried out by Hosokawa (1953), Kopal (1980), and most recently by Ohta, Taruya, & Suto (2005; OTS hereafter). The latter authors derived analytic expressions for the case of planetary transits, and suggested that λ could be determined within a few degrees if high-precision ($\sim 5 \text{ m s}^{-1}$) radial velocity measurements were obtained throughout a transit.

Such high precision can only be achieved for bright stars, and the brightest star that is known to host a transiting planet is HD 209458 (Henry et al. 2000, Charbonneau et al. 2000). This remains the only exoplanetary system for which the RM effect has been detected. Three different groups have reported detections: Queloz et al. (2000), Bundy & Marcy (2000), and Snellen (2004). Most pertinent to this paper is the work of Queloz et al. (2000), who measured the apparent radial velocity of the star during a planetary transit with a precision of 10 m s^{-1} , finding λ to be consistent with zero within about 20° , and $v \sin I_\star = 3.75 \pm 1.25 \text{ km s}^{-1}$ along the transit chord.¹ Since this pioneering work, a treasure-trove of new data has become available, including transit photometry with 10^{-4} precision (Brown et al. 2001), radial velocity measurements with 3–4 m s^{-1} precision (Laughlin et al. 2005), and a recent measurement of the time and duration of the secondary eclipse (Deming et al. 2005).

The motivation for the work described in this paper was to investigate the degree to which the RM analysis could be improved using a combination of these high-precision data. We have also taken the opportunity to update the determinations of the other stellar, planetary, and orbital parameters, on the basis of the joint analysis of radial velocity measurements, photometry, and the timing of the secondary eclipse.

The data on which our analysis is based are described in the following section. The model that was used to fit the data is described in § 3, including a new and empirical method to calculate the anomalous radial velocity due to the RM effect. In § 4 we present the results, showing in particular that the uncertainties in λ and $v \sin I_\star$ have been reduced by an order of magnitude. We also remark on the determination of the orbital eccentricity, a parameter that has been of particular interest ever since Bodenheimer, Lin, & Mardling (2001) pointed out that ongoing eccentricity damping could produce enough tidal heating to account for the unexpectedly large size of the planet. Finally, in § 5 we place the RM results in the context of theories of tidal interactions between planets and their parent stars, and consider the possible significance of this unusually direct means of measuring the projected rotation speed of the star.

2. The Data

Our work is based on three types of data: (1) radial velocity measurements of the parent star throughout its entire orbit, including the transit phase; (2) optical photometry of the system during the transit phase; (3) infrared photometry of the system during secondary eclipse (the phase when the planet is behind the star). We have not obtained any new data. Instead, we have chosen the highest-precision data that are currently available in each of these categories.

2.1. Radial velocities

Our radial velocity measurements are from Laughlin et al. (2005), who used the Keck I 10 m telescope and the High Resolution Echelle Spectrograph (HIRES) equipped with an iodine cell for accurate wavelength calibration. A total of 85 spectra were acquired between November 1999 and December 2004. They were generally taken at random orbital phases, with the notable exception of UT 2000 July 29, when a sequence

¹Bundy & Marcy (2000) detected the effect but did not have enough transit data to justify a thorough analysis. Snellen (2004) had a different motivation. He assumed $\lambda = 0^\circ$ and attempted to detect absorption lines in the atmosphere of the planet through the wavelength dependence of the RM effect.

of 17 spectra was acquired during a transit. This transit-phase subset is obviously important for this work. The rest of the data is also important, because the Keplerian orbit must be known with high accuracy in order for the radial velocity anomaly to be isolated and interpreted. We did not use the three spectra that were taken during ingress or egress because our model for the RM effect, which is presented in § 3.3, is least accurate during the partial phases of the transit.

The radial velocities were derived from the spectra using the technique described by Butler et al. (1996), and have a typical measurement error of 3–4 m s^{−1}. The zero point of the radial velocity scale is arbitrary. As noted by Laughlin et al. (2005), a star such as HD 209458 should produce intrinsic radial velocity noise with a standard deviation of approximately 2.8 m s^{−1}, an empirical estimate based on radial-velocity and chromospheric monitoring of similar stars (Saar, Butler, & Marcy 1998). This intrinsic noise, often referred to as “stellar jitter,” presumably arises from motions or flux variations of the stellar surface. For this reason, as an estimate of the total uncertainty in each radial velocity, we added 2.8 m s^{−1} in quadrature to the quoted measurement error.

2.2. Transit photometry

Our photometry is from Brown et al. (2001), who used the *Hubble Space Telescope* and the Space Telescope Imaging Spectrograph (STIS), sadly now defunct, to record the flux of HD 209458 within a ≈50 nm band centered on 610 nm. They achieved the extraordinary precision of 10^{−4} in relative flux by using STIS as a dispersive photometer. The resulting photometric time series is divided into 20 segments: on each of four occasions (“visits”), the star was observed for five orbits of the telescope around the Earth. The visits were chosen to span particular transit events in 2000 April and May.

The first two orbits and the last orbit of each visit took place when the planet was not transiting. Those data served only to establish the flux baseline for the time variations observed in the third and fourth orbits of each visit. Following Brown et al. (2001), we excluded from consideration the data from the first orbit of each visit, reasoning that they are unnecessary and perhaps even undesirable because the telescope and instrument need time to settle into maximum stability. We also excluded all the data from the first visit, because those data were affected by an instrumental problem (see Brown et al. 2001, § 2). The resulting data set consists of 417 measurements of relative flux, including excellent coverage of the entire transit phase.

2.3. Secondary eclipse timing

The only successful detection of the secondary eclipse was recently achieved by Deming et al. (2005), who monitored the 24 μm flux of the system with the Multiband and Imaging Photometer aboard the *Spitzer Space Telescope*. They detected the diminution of total flux when the planet was hidden by the star, with a total signal-to-noise ratio of 5–6. For our purpose, direct modeling of the light curve is not very useful because of the low signal-to-noise ratio of each data point. However, measurements of the time and duration of the secondary eclipse are potentially useful in determining the orbital eccentricity (e) and argument of pericenter (ω). The following expressions are valid to first order in e :

$$e \cos \omega = \frac{\pi}{2P} \left(t_{\text{II}} - t_{\text{I}} - \frac{P}{2} \right) \quad (1)$$

$$e \sin \omega = \frac{\Theta_{\text{I}} - \Theta_{\text{II}}}{\Theta_{\text{I}} + \Theta_{\text{II}}}, \quad (2)$$

where t_I and t_{II} are the midpoints of the primary eclipse (transit) and secondary eclipse, respectively, and Θ_I and Θ_{II} are the corresponding durations. The orbital period is P . Using t_{II} measured by Deming et al. (2005) and t_I measured by Brown et al. (2001), we find

$$e \cos \omega = (-0.6 \pm 3.7) \times 10^{-3}, \quad (3)$$

which adds a little information beyond what can be learned from the radial velocities and transit photometry alone (see § 4). The constraint on $e \sin \omega$ is not useful, because of the relatively large fractional uncertainty in Θ_{II} . We estimated Θ_{II} from Fig. 1b of Deming et al. (2005) and found

$$e \sin \omega = -0.02 \pm 0.19, \quad (4)$$

which is not sufficiently precise to improve on the constraints from the spectroscopic orbit (Mazeh et al. 2000, Laughlin et al. 2005).

3. Description of the Model

3.1. The Orbit

The basis of the model is a two-body Keplerian orbit (see Fig. 1). The orbit is specified by the masses of the star and planet (M_\star and M_p), the orbital period (P), the orbital eccentricity (e), the argument of pericenter (ω), the orbital inclination (I), and the radial velocity of the center of mass (γ).² Given the initial condition, it is a venerable and straightforward problem to compute the sky position (X, Y) and radial velocity \dot{Z} of the center of mass of either body at any subsequent time. We chose to parameterize the initial condition by the free parameter Δt_I , defined as

$$\Delta t_I \equiv t_I - 2,451,659.93675, \quad (5)$$

where t_I is the central transit time, measured in heliocentric Julian days. The reference time is the central transit time measured by Brown et al. (2001). We did not allow P to vary, since it has been determined independently with much greater precision than can be achieved with only the data analyzed here. We adopted the value $P = 3.52474895$ days, which is based on an analysis of the STIS data by Brown et al. (2001) and a subsequent series of STIS observations by Charbonneau et al. (2003). The uncertainty in P is 83 ms which is negligible for our purposes (see § 4.1).

3.2. The Flux

There are two more parameters for the planetary radius (R_p) and stellar radius (R_\star). The transit occurs when the sky position of the planet is less than $R_p + R_\star$ away from the sky position of the star, and $Z_\star > Z_p$. Outside transit, the model flux is unity. During transit, the model flux is computed under the assumption of a quadratic limb-darkening law,

$$\frac{I(\mu)}{I(1)} = 1 - u_1(1 - \mu) - u_2(1 - \mu)^2, \quad (6)$$

²Laughlin et al. (2005) reported only the radial velocity variations relative to an arbitrary velocity standard. Our model parameter γ is the offset between this zero point and the heliocentric radial velocity of the center of mass.

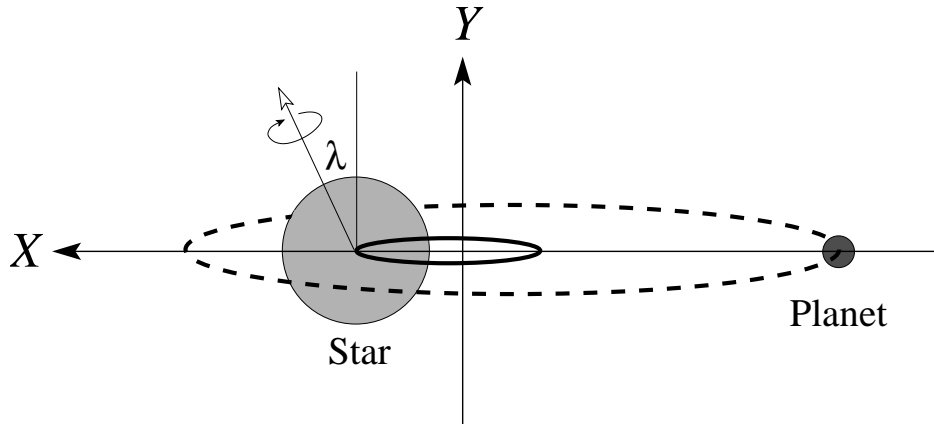


Fig. 1.— Coordinate system of the model. The X - Y plane is the sky plane. The Z axis points away from the observer. The projected stellar orbit is shown by the solid ellipse, and the projected planetary orbit is shown by the dashed ellipse. Without loss of generality, the longitude of nodes is chosen to lie along the X axis. The argument of pericenter is zero in this illustration, but it is a free parameter in the model. The angle λ is between the Y axis and the sky projection of the stellar rotation axis.

using the algorithm of Mandel & Agol (2002). In this expression, μ is the cosine of the angle between the line of sight and the normal to the stellar surface. The two numbers u_1 and u_2 are free parameters. This is the same parameterization that was used by Brown et al. (2001).

3.3. The Radial Velocity

Outside transit, the model radial velocity of the star is $\gamma + \dot{Z}$. During transit, we must take into account the RM effect. We write the model radial velocity as $\gamma + \dot{Z} + \Delta v$, where Δv is the anomalous Doppler shift. The value of Δv obviously depends on the position of the planet and the rotation rate of the star, but what is the exact dependence? Since this is the heart of the matter, we devote extra attention to this aspect of the model.

Queloz et al. (2000) interpreted their radial velocity measurements using a finite-element model of the star. They divided the stellar disk into 90,000 cells and calculated the expected surface brightness and spectral line profile from each cell individually. Then, to simulate a transit spectrum, they summed the spectra of the cells that are not obstructed by the planet, weighted by the relative intensities of the cells. Finally, to compute Δv , they measured the apparent Doppler shift of this simulated spectrum, presumably using the same reduction pipeline that they used on the actual data.

Ohta, Taruya, & Suto (2005) derived an analytic formula for Δv as a function of the planet position and stellar rotation rate. Using an analytic formula is much easier and computationally faster than using a finite-element model. However, we were concerned that the OTS formula is based on a premise that may not apply in this case. The spectral distortion due to the RM effect is the subtraction of a small fraction $[\propto (R_p/R_\star)^2]$ of a narrow range of velocities from the rotationally-broadened line profile. The OTS formula gives the first moment of the distorted line profile (the “center of gravity” in wavelength space). Intuitively, one would expect the first moment to be a good approximation to the measured Doppler shift, but the Butler

et al. (1996) method is not specifically designed to measure the first moment of spectral lines. Rather, it is designed to find the optimal value of an overall wavelength shift that brings the observed spectrum and a template spectrum into best agreement, while also fitting for many other free parameters describing variations in the instrumental response. This method is not the same as measuring a first moment; in particular, it assumes that any spectral distortion is instrumental. When presented with an intrinsically distorted transit spectrum, the degrees of freedom that are intended to mimic instrumental changes may absorb some of the true signal. For this reason, the applicability of the OTS formula is not assured.

Our approach to this problem was to test the OTS formula in a manner similar in spirit to the technique of Queloz et al. (2000). We simulated Keck/HIRES spectra taken during a transit; then, we “measured” Δv from these simulated spectra using the same reduction pipeline that was used by Laughlin et al. (2005); and finally, we compared the results with the predictions of the OTS formula. The details were as follows. We began with the NSO solar spectrum (Kurucz, Furlenid, & Brault 1984), which for our purposes has effectively infinite resolution, and performed the following steps:

1. Broaden the NSO spectrum to mimic the disk-integrated spectrum of HD 209458. The convolution kernel was chosen so that the broadened spectrum had a line width of 4.5 km s^{-1} , the value measured by Fischer & Valenti (2005) for HD 209458, and was computed assuming a linear limb-darkening law appropriate for the star’s color and the mean wavelength of the relevant spectral region ($u_1 = 0.6$, $u_2 = 0$; Gray 1992). Call this spectrum S_\star .
2. Begin again with the NSO spectrum at the native (unbroadened) line width. Scale it by an overall factor f , Doppler-shift it by an amount $\Delta\lambda/\lambda = v_p/c$, and refer to the result as S_p . This is meant to represent the spectrum of the occulted portion of the stellar disk: f is the flux of the occulted portion, and v_p is the mean line-of-sight velocity (the “sub-planet” velocity) of the occulted portion.
3. Compute $S_{\text{tr}} = S_\star - S_p$, where “tr” indicates “transit.” This is the simulated transit spectrum at infinite resolution.
4. Multiply S_{tr} by the measured iodine absorption spectrum, which is also effectively of infinite resolution.
5. Convolve the result with a model point-spread function that is derived from actual Keck/HIRES observations of HD 209458, and store the result in the same digital format as reduced Keck/HIRES spectra.
6. Use the result as input to the same Doppler-shift measuring algorithm that was employed on the actual Keck/HIRES spectra. Record the result as Δv .

This procedure does not account for any time variations of f and v_p during the spectroscopic exposure, but OTS have shown that such time variations are negligible for exposure times less than 10 minutes. We performed the preceding steps for different choices of the input parameters f and v_p , producing a two-dimensional grid of results $\Delta v(f, v_p)$. We allowed f to vary from zero to 0.02, and v_p to vary from -4.5 to $+4.5 \text{ km s}^{-1}$. The resulting surface is very well described by a polynomial approximation,

$$\Delta v = -f v_p \left[1.33 - 0.483 \left(\frac{v_p}{4.5 \text{ km s}^{-1}} \right)^2 \right], \quad (7)$$

with differences smaller than 0.5 m s^{-1} between the grid values and the polynomial approximation.

In order to compare the OTS formula with the results of our simulations, we calculated Δv at each step of a planetary transit, using each of the two schemes. We adopted parameters for the planet and the star that are similar to those of the HD 209458 system. At each moment during the transit, we used the OTS formula to calculate Δv as a function of the planet coordinates. We also computed f using the limb-darkening law of Eq. (6), and v_p assuming solid-body rotation for the star, which then allowed us to calculate Δv using Eq. (7). Figure 2 compares the results of the two different methods of determining Δv , as a function of the X coordinate of the planet. The OTS formula is a reasonable approximation of the simulated results, but it underpredicts the magnitude of Δv by approximately 10%.

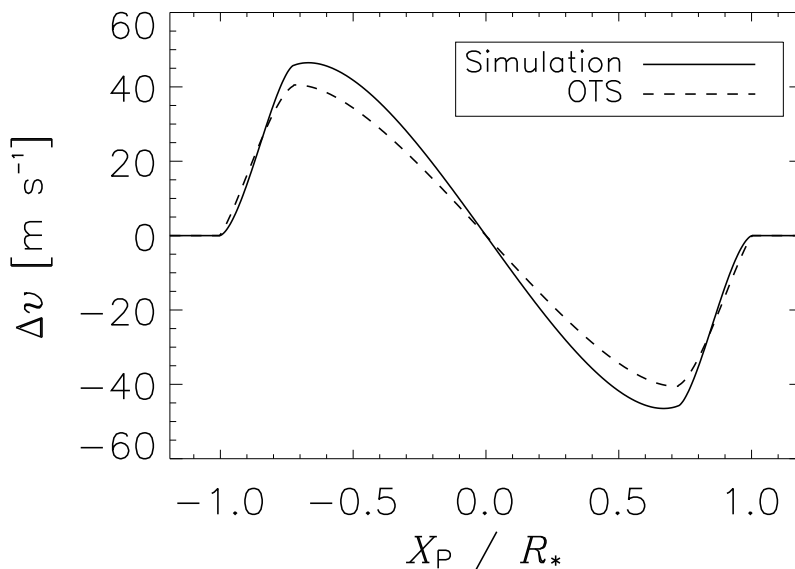


Fig. 2.— The radial velocity anomaly due to the Rossiter-McLaughlin effect, as calculated *via* our simulations (solid line) and the formula of Ohta et al. (2005) (dashed line). The horizontal axis is the distance from the planet to the projected axis of the stellar spin. The orbital, planetary, and stellar properties were chosen to be approximately those of HD 209458: $R_p/R_\star = 0.12$, $Y_p/R_\star = 0.5$, $e = 0$, $\lambda = 0^\circ$, $v \sin I_\star = 4.5 \text{ km s}^{-1}$, and $u_1 + u_2 = 0.64$.

We do not know the cause of the discrepancy, apart from the general argument presented earlier that the quantity calculated by OTS is not the quantity that is truly measured by the algorithm of Butler et al. (1996). In fact, we expected the OTS formula to *overestimate* the magnitude of Δv , given our previous argument that some of the free parameters in the Butler et al. (1996) algorithm might act to dilute the signal. We believe that our simulations provide a better representation of the true measurement, and hence, we employed Eq. (7) in our model of the RM effect. However, as mentioned in § 2.1, we did not attempt to fit the three radial velocity measurements that were taken during an ingress. This is because during the partial transit phases, the planet is closest to the stellar limb, which is when unmodeled physical effects are most pronounced. Such effects include departures from quadratic limb darkening, variations of the limb darkening across the area covered by the planet, and any intrinsic center-to-limb variations of the line profile, including the “convective blue shift” (Beckers & Nelson 1978).

In summary, the radial velocity anomaly of the model is calculated as follows. At a given time during a transit, the positions of the star and planet are determined, and f is computed with the procedure described above. The sub-planet velocity v_p is computed by assuming solid-body rotation of the star (an assumption whose validity is considered briefly in § 5). Then, Eq. (7) is used to calculate Δv . The description of the RM effect adds two additional free parameters to the model: $v \sin I_*$ of the stellar rotation, and λ , the angle between the sky-projected axes of the planetary orbit and the stellar rotation (see Fig. 1).

4. Fitting Procedure and Results

The model has 13 free parameters, but only 12 of these parameters can be determined independently. There is a well known degeneracy between M_* , M_p , and R_* as determined from transit data. We chose to fix the value of M_* and optimize all the other parameters. We repeated the optimization for three different choices of M_*/M_\odot : 0.93, 1.06, and 1.19. These values span the full range of possibilities that Cody & Sasselov (2002) concluded is reasonable for HD 209458.

We used an AMOEBA algorithm (Press et al. 1992) to minimize

$$\chi^2 = \sum_{n=1}^{N_v} \left(\frac{v_O - v_C}{\sigma_v} \right)^2 + \sum_{n=1}^{N_f} \left(\frac{f_O - f_C}{\sigma_f} \right)^2 + \left(\frac{t_{\text{II},O} - t_{\text{II},C}}{\sigma_t} \right)^2 \quad (8)$$

as a function of all the parameters. Here, v_O and v_C are the observed and calculated radial velocities, of which there are $N_v = 83$ (14 during the transit phase). Likewise, f_O and f_C are the observed and calculated fluxes, of which there are $N_f = 417$. The final term in the sum represents the constraint on the time of secondary eclipse.

For $M_*/M_\odot = 1.06$, the best-fitting model has $\chi^2 = 528$, with 489 degrees of freedom ($\chi^2/N_{\text{DOF}} = 1.08$). We consider this an excellent fit. The data and the best-fitting model are compared in Fig. 3. The RM effect is apparent as the sinusoidal glitch in the radial velocity curve near zero phase. The three radial velocity measurements that were taken during ingress (and which were not used in the fitting procedure) are plotted with open circles.

To estimate the uncertainties in the parameters, we performed a bootstrap Monte Carlo analysis as described by Press et al. (1992). We created synthetic data sets, each of which had the same N_v and N_f as the actual data set. Each entry in a synthetic data set was a datum (a calendar date and the value of the flux or radial velocity measured on that date) drawn randomly from the real data set, with repetitions allowed. Thus, a substantial fraction of the entries in each synthetic data set are duplicated at least once, and receive greater weight in the χ^2 sum. The idea is to estimate the probability distribution of the data using the observed data values themselves, rather than choosing models for the underlying physical process and for the noise. For each of the three different choices of M_* , we created 10^5 synthetic data sets, and re-optimized the 12 free parameters for each synthetic data set. The resulting distribution of best-fitting parameters was taken to be the joint probability distribution of the true parameter values.

Table 1 gives the mean value of each parameter, the standard deviation, and the estimated 90% confidence limits. In addition to the model parameters, results are given for some related derived quantities, such as R_p/R_* and $e \cos \omega$. Most of the results in Table 1 were based on the histograms of all 3×10^5 results, i.e., they incorporate the uncertainty in the stellar mass. For those parameters whose uncertainties are dominated by the uncertainty in stellar mass, results are also given for the particular case $M_*/M_\odot = 1.06$, to show how much the uncertainty would be reduced with perfect knowledge of the stellar mass.

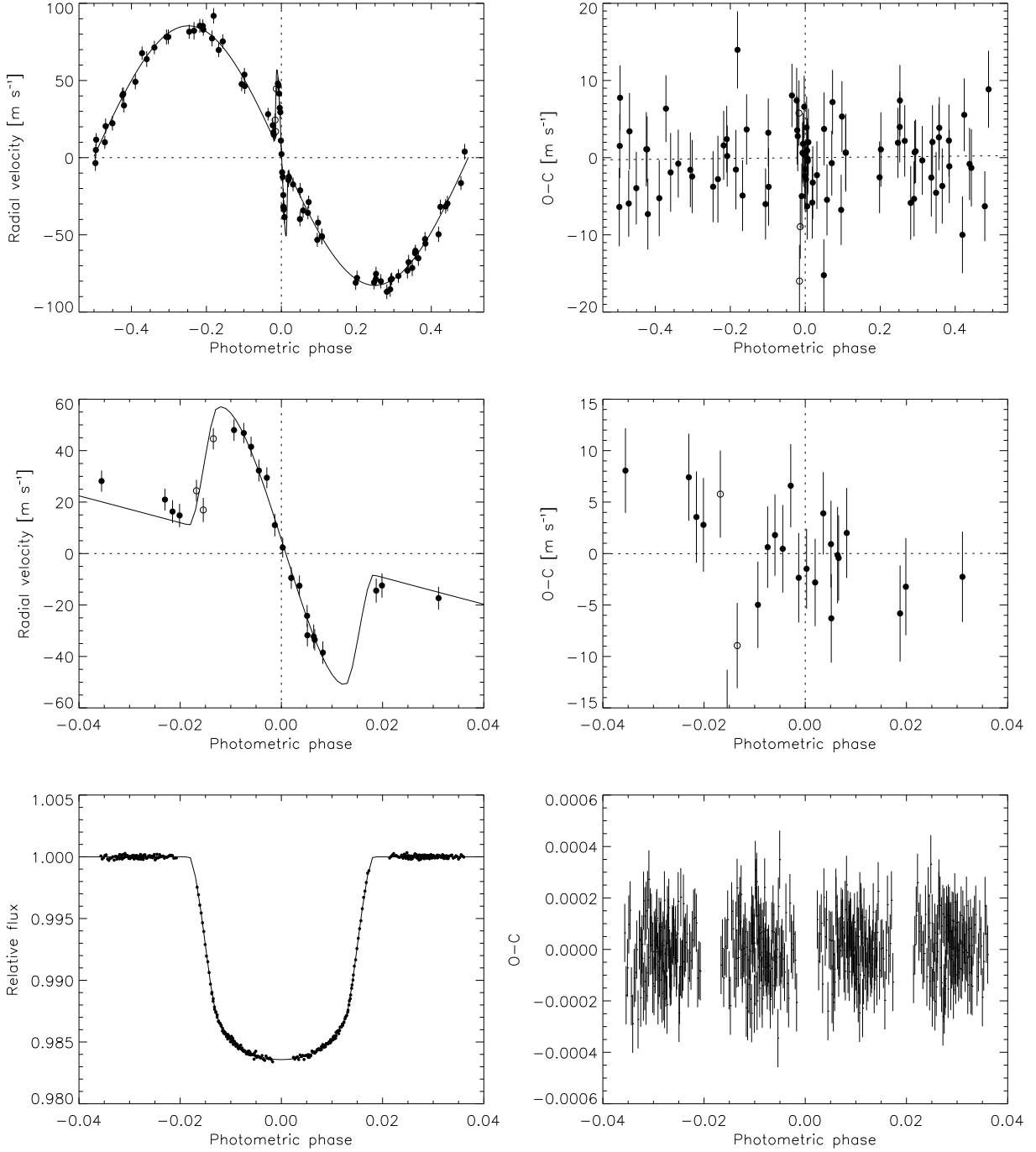


Fig. 3.— Comparison of the data and the best-fitting model, for the case $M_*/M_\odot = 1.06$. The left panels show the data (points) and the model (line), as a function of photometric phase. The right panels show the residuals (observed minus calculated). *Top row.*—The radial velocity data. *Middle row.*— Close-up of the radial velocity data near the transit phase, including 3 points (open circles) that were not used in the fitting procedure. *Bottom row.*—Photometry.

Some of the parameters have correlated uncertainties. Figures 4–6 show most of these correlations, for the particular choice of stellar mass $M_\star/M_\odot = 1.06$. Each panel shows the 12-dimensional probability distribution function projected onto a two-dimensional plane in parameter space. The isoproability contours enclosing 68% of the results are plotted, to show the approximate “1 σ ” joint confidence regions for the two plotted parameters. In the remainder of this section, we call attention to some of the principal results.

4.1. The Rossiter-McLaughlin effect

We find $v \sin I_\star = (4.70 \pm 0.16)$ km s^{−1} for the line-of-sight rotation speed of the star at the latitude crossed by the planet.³ This result is in agreement with (but is more precise than) the value 3.75 ± 1.25 km s^{−1} found by Queloz et al. (2000). This number is primarily determined by the amplitude of the radial velocity anomaly and the depth of the transit, as interpreted through Eq. (7). If the OTS formula is used instead of Eq. (7), then we obtain $v \sin I_\star = 6.0$ km s^{−1}; but, as discussed in § 3.3, the applicability of the OTS formula to these data is questionable.

We find $\lambda = -4.4 \pm 1.4$, a small but significantly nonzero angle. How robust is this result? This number is primarily determined by the time interval between two events: the moment when the radial velocity anomaly vanishes [$t(\Delta v = 0)$], and the moment of greatest transit depth (t_1). As long as $I \neq 90^\circ$ and $I_\star \neq 0^\circ$, then

$$\lambda = 0 \iff t(\Delta v = 0) = t_1. \quad (9)$$

Thus, our ability to test whether or not λ is zero depends chiefly on our ability to assign consistent orbital phases to all the radial velocities and photometry obtained during transits. It depends secondarily on the radial velocities measured outside transits, since those data determine the Keplerian orbit and allow the radial velocity anomaly to be isolated. It does *not* depend critically on our models for the limb darkening or the RM effect; in any reasonable limb-darkening model, t_1 occurs when the projected planet–star separation is smallest, and in any reasonable RM model, $t_{\Delta v=0}$ occurs when the planet crosses the projected stellar rotation axis.

In the best-fitting model, shown in Fig. 3, one can see that the model radial velocity curve passes close to the origin, but that there is a small offset between zero radial velocity variation and zero photometric phase. The time interval $t(\Delta v = 0) - t_1$ is 4.3 minutes. This timing offset is not caused by the uncertainty in the orbital period P . The elapsed time between the transit photometry and the transit subset of radial velocities was approximately 3 months, or 25 orbits. The 83 ms uncertainty in P causes an uncertainty of only ~ 2 seconds in lining up the radial velocity and the flux data, which is much smaller than 4.3 minutes. Even over the 5 yr time span of all the Laughlin et al. (2005) measurements, the maximum phase offset due to the uncertainty in P corresponds to a timing offset of only 43 seconds. If we fix $\lambda = 0^\circ$ and allow P to vary to best fit the data, we find $P = 3.52472441$ days, which is 25σ larger than the externally measured period.

A more serious concern than the uncertainty in P is the possibility that the transit radial velocity measurements are all systematically high because of stellar jitter. The time scales and corresponding amplitudes of these random radial velocity excursions are poorly known, but if the star happened to experience an

³It might appear that this result represents an extrapolation beyond the grid of $\Delta v(f, v_p)$ that was the basis of Eq. (7), but this is not so. For a transit at stellar latitude b and $\lambda \approx 0$, the maximum sub-planet velocity is $v_p = v \sin I_\star \cos b$. In this case, $b \approx 30^\circ$, and the maximum v_p is 4.1 km s^{−1}, whereas our grid extended up to 4.5 km s^{−1}.

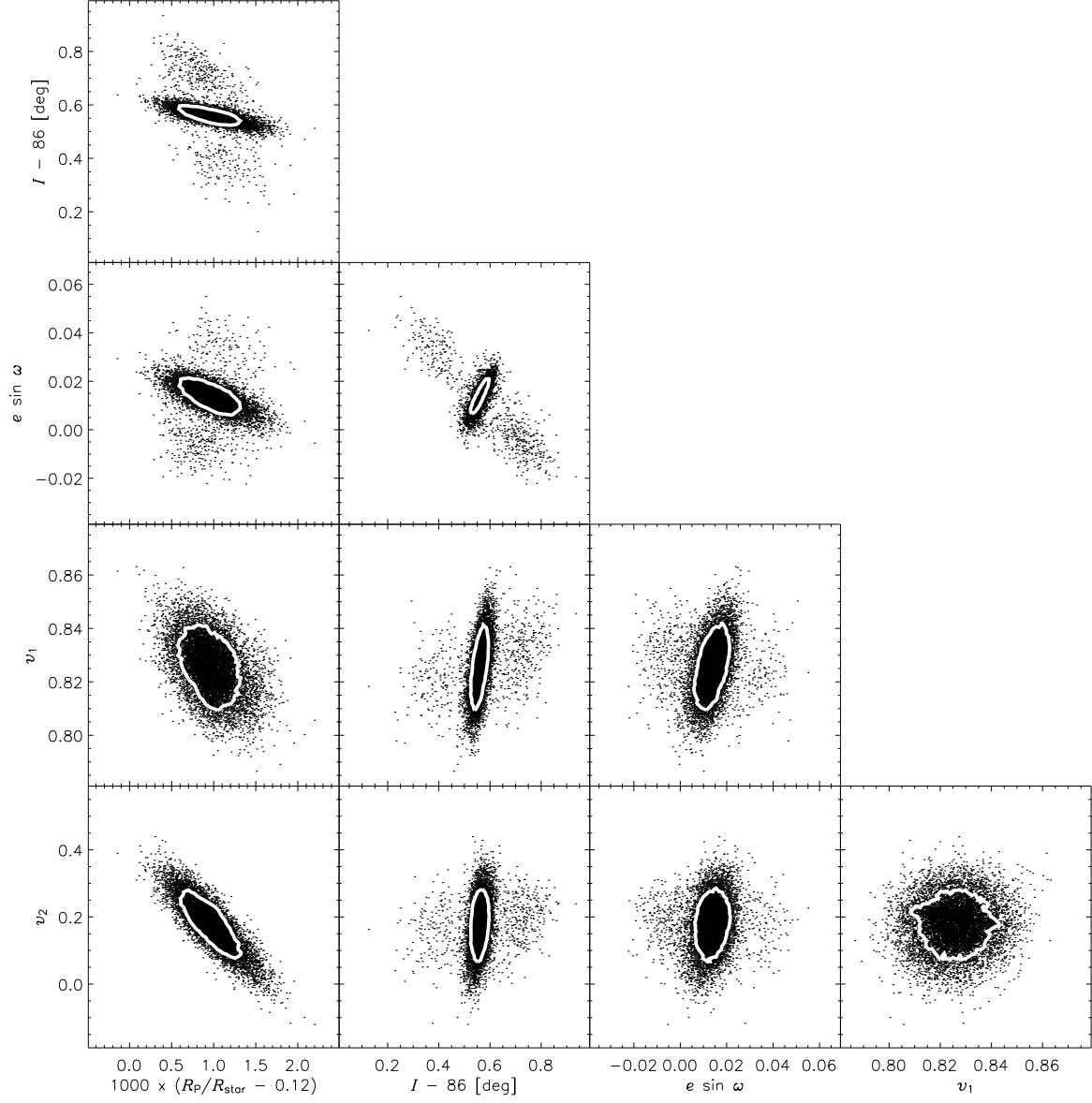


Fig. 4.— Joint probability distributions of some planetary, stellar, and orbital parameters. The density of points is proportional to the probability density. The white lines are isoprobability contours enclosing 68% of the points. Results are shown for the specific choice $M_*/M_\odot = 1.06$, but none of the distributions plotted varies significantly with stellar mass. The parameters shown here are determined mainly by the photometry.

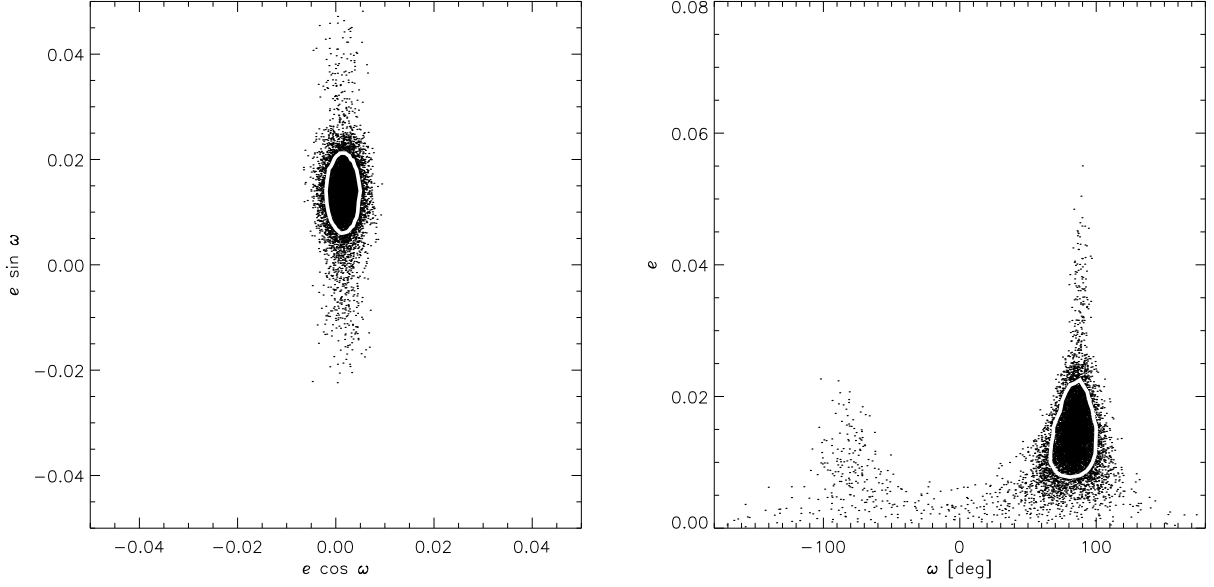


Fig. 5.— Same as Fig. 4, but for parameters relating to the orbital eccentricity. The nonzero result for $e \sin \omega$ is probably an artifact of the limb-darkening model (see §4.4).

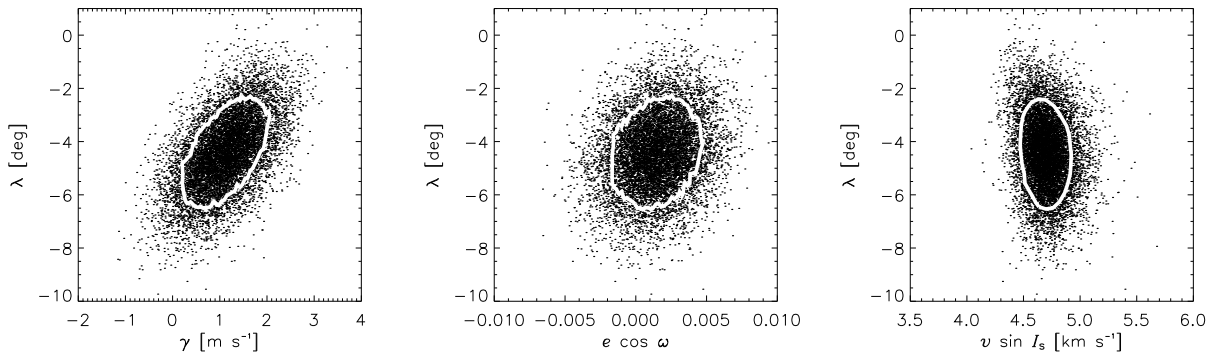


Fig. 6.— Same as Fig. 4, but for parameters relating to the Rossiter-McLaughlin effect.

excursion of $\sim 5 \text{ m s}^{-1}$ during the entire night of the transit of 2000 July 29, then our conclusion regarding a nonzero λ would be erroneous. The only way to settle this matter would be to obtain additional radial velocity measurements during transits.

Two of the model parameters have variances that are notably correlated with the variance in λ . One of them is γ , the velocity zero point, which is easily understood since $t(\Delta v = 0)$ depends on γ . The second correlated parameter is $e \cos \omega$, which is relevant because it controls the timing offset between the moment when the Keplerian radial velocity variation vanishes, and the moment when the anomalous Doppler shift vanishes. These correlations are shown in Fig. 6. Also plotted is the joint distribution of $v \sin I_*$ and λ , showing that the variances in those parameters are not correlated.

4.2. The masses and radii

The best-fitting values for the mass and radius of the planet, and for the radius of the star, are given in Table 1. The uncertainties in these quantities are dominated by the uncertainty in the stellar mass. These well-known degeneracies can be written $M_p \propto M_*^{2/3}$, $R_p \propto M_*^{1/3}$, and $R_* \propto M_*^{1/3}$. The ratio of radii does not depend on M_* and is determined with high accuracy from the photometry. Cody & Sasselov (2002) used theoretical models of stellar structure and evolution to show that R_* is a *decreasing* function of M_* , for fixed values of the star’s observable properties (luminosity, effective temperature, and metal abundance). If one were willing to use the theoretical models to set *a priori* constraints on the mass–radius relationship, then the degeneracy would be partially broken.

4.3. The limb darkening

The two parameters that describe the limb darkening are u_1 and u_2 . The uncertainties in these parameters are highly correlated, and one linear combination of these parameters is much more tightly constrained than the orthogonal combination. The appropriate linear combinations are

$$v_1 \equiv u_2 + \frac{5}{3}u_1 = 0.83 \pm 0.01, \quad (10)$$

$$v_2 \equiv u_2 - \frac{3}{5}u_1 = 0.18 \pm 0.07. \quad (11)$$

The variances of these parameters are uncorrelated (see Fig. 4). For this reason, Table 1 gives the results for v_1 and v_2 rather than for u_1 and u_2 . In contrast, Brown et al. (2001) presented results for the parameters $u_1 + u_2$ and $u_1 - u_2$, which we find to be correlated. Some further remarks on the effect of limb darkening are given below.

4.4. The orbital eccentricity

The 90% confidence upper limit on the eccentricity is $e < 0.023$. This agrees with the upper limit that was achieved by Laughlin et al. (2005) using only the radial velocity data. But are the data consistent with zero eccentricity? The answer to this question is important because, as mentioned in § 1, the observation of a nonzero eccentricity might help to solve the mystery of why the planet’s density is much smaller than the density of Jupiter (Bodenheimer et al. 2001). Formally, we find $e > 0.0057$ with 90% confidence (see Fig. 5),

but this result is highly suspect. We believe that the data are actually consistent with zero eccentricity, and that the lower bound on e is an artifact of our imperfect limb-darkening model. Although this problem does not affect the RM results or any of the discussion on which they are based (§ 5), we digress here to explain the problem in more detail, and suggest how to correct it in future analyses.

The natural parameters for describing departures from circularity are $e \cos \omega$ and $e \sin \omega$, because the errors in these parameters are uncorrelated, whereas e and ω are correlated (see Fig. 5). In addition, the determination of e is biased because e must be positive; random errors in measurements of a circular orbit can only increase the apparent eccentricity. In contrast, $e \cos \omega$ and $e \sin \omega$ can assume positive or negative values. The quantity $e \cos \omega$ is independently constrained by the measurement of the time of the secondary eclipse (§ 2.3), and is consistent with zero with a small uncertainty. The quantity $e \sin \omega$ controls the speed of the planet during transit and thus the duration of the transit (the time between first and last contacts). However, the measured duration also depends on several other parameters, namely R_p , R_\star , I , u_1 and u_2 . A bias in any of these parameters produces a corresponding bias in $e \sin \omega$.⁴ In particular, if the quadratic limb-darkening law is not a perfect description of the true limb darkening, then $e \sin \omega$ can be adjusted to compensate for the imperfection.

If $e \cos \omega = 0$ and $e \sin \omega$ is nonzero due to such a bias, then relatively large values of e are allowed when ω is nearly 90° or -90° . This is precisely what is seen in Fig. 5. The high- e solutions are also evident in Fig. 4 as the extended “wings” in the probability distributions of the parameters that are correlated with $e \sin \omega$. We confirmed that different choices for the limb-darkening law result in significantly different values for $e \sin \omega$. In short, the quoted uncertainties for the parameters that describe the photometry are internal to our choice of limb-darkening law. Because the present work is concerned mainly with λ and $v \sin I_\star$, which are not correlated with any of those parameters, we have not attempted to correct this bias. One could do so by adopting a more accurate or a more general model for limb darkening, and by incorporating multi-color photometry rather than the monochromatic photometry analyzed here. Alternatively, once it becomes possible to measure the duration of secondary eclipse with much greater precision, Eq. (2) can be used to place a direct constraint on $e \sin \omega$ (though there may be a related bias in that measurement as well).

5. Summary and Discussion

Through a joint analysis of all the best measurements of HD 209458 that are available, we have estimated the orbital, stellar, and planetary parameters and their uncertainties. Our results agree with previous determinations of these parameters by investigators who analyzed subsets of these data, and in some cases we have modestly decreased the uncertainties (cf. Brown et al. 2001, Deming et al. 2005, Laughlin et al. 2005). The greatest improvement was achieved for the parameters describing the Rossiter-McLaughlin effect, $v \sin I_\star$ and λ , for which the uncertainties have been decreased by a factor of 10 relative to the results of Queloz et al. (2000). This was accomplished by employing higher-precision radial velocity measurements and by interpreting these measurements with a new modeling technique.

The angle λ is measured between the sky projections of two vectors: \mathbf{L}_p , the orbital angular momentum of the planet; and \mathbf{L}_\star , the rotational angular momentum of the star. Thus, λ is a lower bound on the three-

⁴Another way to describe the situation is that when e is small and $\omega = \pm 90^\circ$, the only observable consequence of $e \neq 0$ is a time-symmetric distortion of the transit light curve: a dilation or compression that is symmetric about the central transit time. Time-symmetric distortions are also produced by varying the inclination and the limb-darkening coefficients, which is why there is a degeneracy between $e \sin \omega$ and those other parameters.

dimensional angle ψ between these two vectors. The relation between λ and ψ depends on the inclinations I and I_\star of the planetary orbit and stellar spin axis:

$$\cos \psi = \cos I_\star \cos I + \sin I_\star \sin I \cos \lambda. \quad (12)$$

Since the orbit is nearly edge-on, this relation can be simplified to $\cos \psi \approx \cos \lambda \sin I_\star$. We expect ψ to be not much larger than λ , unless the star’s axis is pointed towards the Earth (a coincidence that is *a priori* unlikely and would also imply a stellar rotation speed v that is considerably faster than expected for a middle-aged G dwarf). In what follows, we suppose that $\psi \lesssim 0.1$ rad, and consider the implications.

This result is reminiscent of the planetary orbits in the solar system. Relative to the net angular momentum vector of the solar system, the rotation axis of the Sun is inclined by 6° , and the orbital angular momentum vectors of individual planets are tipped by $3\text{--}10^\circ$. The planet orbiting HD 209458 is similar to solar system planets in this respect, even though it is much closer to its parent star than any of the planets in the solar system. Its orbital distance is only about 9 stellar radii, as compared to 83 stellar radii for the orbit of Mercury. In this sense, our result extends by a factor of 9 the range of orbital distances over which spin-orbit alignment has been measured.

This proximity to its parent star raises the question of whether any novel spin-orbit interactions can be observed in the HD 209458 system that are not observed in the solar system. Miralda-Escudé (2002) considered the interaction between a close-in giant planet and its parent star’s gravitational quadrupole field. If the planetary orbit is inclined, the line of nodes of the orbit regresses. This effect is potentially measurable as a slow secular variation in the duration of transits. The precession frequency is

$$\dot{\Omega} = - \left(\frac{2\pi}{P} \right) \left(\frac{R_\star}{a} \right)^2 \left(\frac{3J_2}{4} \right) \left(\frac{\sin 2\psi}{\sin \psi_p} \right), \quad (13)$$

where a is the semimajor axis of the planetary orbit (in this case, $a/R_\star = 8.65$), J_2 is the dimensionless quadrupole moment of the star, and ψ_p is the angle between \mathbf{L}_p and $\mathbf{L}_p + \mathbf{L}_\star$. Assuming $J_2 \sim 10^{-6}$ (a few times larger than the Sun’s quadrupole moment), the precession rate for HD 209458 is $\sim 4'' \text{ yr}^{-1}$, corresponding to a precession period of 6×10^7 orbital periods. Successive transits should vary in duration by a fractional amount $\sim 10^{-8}$. This is a minuscule effect, but it may nevertheless be detectable with high-precision photometry spanning several years (see Miralda-Escudé 2002, § 2.3).

Tidal interaction between the star and planet should also be considered. The planet raises a tide on the star, and vice versa. These tides dissipate energy, and the tidal bulges of one body exert torques on the other body. Rasio et al. (1996) showed that the orbit of 51 Peg b (a typical close-in giant planet) is formally unstable to tidal decay, but also that the timescale for orbital shrinkage is longer than the main-sequence lifetime of the parent star. Likewise, tidal dissipation acts to coplanarize the orbit and the stellar equator (Greenberg 1974; Hut 1980), but we show presently that the timescale for this process is longer than the age of the system. Using a simplified model of tidal friction, Hut (1981) calculated the time evolution of a general two-body orbit. Specializing to the case $e = 0$, and considering first only the tide raised on the star by the planet, the equation governing the evolution of ψ can be written (to first order in ψ):

$$\frac{1}{\psi} \frac{d\psi}{dt} = - \frac{3k}{4\pi r_g^2 Q_\star} \left(\frac{GM_\star}{R_\star^3} P_\star \right) \left(\frac{M_p}{M_\star} \right)^2 \left(\frac{R_\star}{a} \right)^6 \left[1 - \frac{1}{2} \left(1 - \frac{L_\star}{L_p} \right) \frac{P}{P_\star} \right], \quad (14)$$

where P_\star is the rotation period of the star; Q_\star is the dimensionless “quality factor” of the tidal oscillations in the star (and is inversely proportional to the dissipation rate); k is the apsidal motion constant ($k \approx 0.01$

for a solar-type star); and r_g is the dimensionless radius of gyration ($r_g^2 \approx 0.1$). From this equation, the characteristic time scale for significant change in ψ is

$$\tau_\psi \sim \left(\frac{4\pi r_g^2 Q_\star}{3k} \right) \left(\frac{R_\star^3}{GM_\star} \frac{1}{P_\star} \right) \left(\frac{M_\star}{M_p} \right)^2 \left(\frac{a}{R_\star} \right)^6 \sim 5 \times 10^{12} \text{ yr} \left(\frac{Q_\star}{10^6} \right), \quad (15)$$

where we have evaluated the expression for the parameters of HD 209458 and a reasonable guess for Q_\star (Terquem et al. 1998). Since the age of the star is only about 5×10^9 yr (Cody & Sasselov 2002), any inclination damping should be negligible. The inclination we have observed is therefore likely to be a relic of the planet formation epoch. Alternatively, our measurement of a nonzero inclination could be considered as a weak upper bound on tidal dissipation, $Q_\star < 10^{10}$.

The star also raises tides on the planet. Through this mechanism, the planet’s rotation period is synchronized with the orbital period and the orbit is circularized on relatively short timescales ($\tau_{\text{synch}} \sim 10^6$ yr and $\tau_{\text{circ}} \sim 10^9$ yr; Rasio et al. 1996). This is why the perturbing effect of a third body is required to maintain a nonzero eccentricity, in the scenario proposed by Bodenheimer et al. (2001). However, if the orbit is inclined relative to the stellar quadrupole, then the planet experiences a time-variable tidal distortion even after synchronization and circularization are achieved. The planet makes a vertical oscillation in the quadrupolar field of the star once per orbit. To investigate whether this oscillation produces a significant amount of heat, we followed the same procedure that Peale & Cassen (1978) used to calculate tidal heating within the Moon, and that Wisdom (2004) recently applied to the case of Enceladus. We identified the leading time-variable term in the tidal potential and calculated the resulting height of the tide, approximating the planet as an incompressible fluid. For the case of HD 209458b, the time-averaged heating rate is

$$\frac{dE}{dt} = 2 \times 10^{11} \text{ erg s}^{-1} \left(\frac{Q_p}{10^6} \right)^{-1} \left(\frac{J_2}{10^{-6}} \right)^2 \left(\frac{\sin \psi}{0.1} \right)^2 = 6 \times 10^{-16} \left(\frac{GM_p^2/R_p}{10^9 \text{ yr}} \right), \quad (16)$$

to leading order in $J_2 \sin \psi$. This heating rate is utterly negligible compared to other sources of heat such as gravitational contraction and stellar insolation. A potentially more powerful source of heat is the tide that would be produced by a nonzero planetary obliquity. For a close-in giant planet with $\psi \neq 0$, it may be possible for the obliquity (the angle between the planetary spin axis and the orbit normal) to avoid being driven to zero during the synchronization process, a theoretical possibility that has been explored by Winn & Holman (2005).

Finally, we turn to the implications of our measurement of the stellar spin, $v \sin I_\star = (4.70 \pm 0.16) \text{ km s}^{-1}$. Because λ is nearly zero, the result can be interpreted as the line-of-sight rotation speed of the star along the stellar latitude traversed by the transiting planet. The stellar spin can also be estimated in the traditional manner, by interpreting the observed broadening of photospheric absorption lines. Fischer & Valenti (2005) did so for HD 209458 using Keck/HIRES spectra, finding $v \sin I_\star = (4.5 \pm 0.3) \text{ km s}^{-1}$. Likewise, Mazeh et al. (2000) reported two estimates of $v \sin I_\star$, (4.4 ± 1.0) and $(4.1 \pm 0.6) \text{ km s}^{-1}$, based on spectra taken with two different instruments, and Shkolnik et al. (2005) found $v \sin I_\star = (4.2 \pm 0.5) \text{ km s}^{-1}$. All these values are in agreement within the quoted uncertainties.

The agreement is potentially interesting for at least three reasons. First, it is a consistency check on our method for interpreting the Rossiter-McLaughlin effect (§ 3.3). Second, assuming that our method is correct, it provides a rare example apart from the Sun for which the traditional interpretation of spectral line broadening can be checked. There are physical effects besides rotation that contribute to line broadening, such as macroturbulence and microturbulence. In general, assumptions must be made about the magnitude of these other effects in deriving $v \sin I_\star$ from the net observed line broadening. Our result shows that for the

case of HD 209458, these assumptions are apparently justified. Finally, if our method and the traditional interpretation of line broadening are assumed to be correct, then the agreement between the two estimates of $v \sin I_*$ places an upper bound on any differential rotation of the star. The line-broadening measurement is a disk-averaged quantity, whereas the transit measurement refers specifically to a latitude of 30° . Together, the two measurements imply $(v_{\text{avg}} - v_{30^\circ}) \sin I_* = -0.20 \pm 0.34 \text{ km s}^{-1}$, corresponding to $(-4.4 \pm 7.6)\%$ of the average rotation speed. Unfortunately, we lack the precision to detect the degree of differential rotation expected of a solar-type star. On the Sun, differential rotation between the equator and latitude 30° is only about 0.1 km s^{-1} , or 5% of the equatorial speed (Beck 2000), and of course the difference between the disk-averaged rotation and the rotation at latitude 30° is even smaller.

In closing, we wish to point out that although HD 209458 is presently the only extrasolar planetary system for which the Rossiter-McLaughlin effect has been detected, it is possible that a large sample of suitable systems will soon be available. A second example of a transiting planet with a bright parent star was recently discovered: TrES-1, whose parent star is a 12th magnitude K dwarf (Alonso et al. 2004). It would be interesting to perform a similar analysis of this system, given the different stellar type and planetary characteristics. Numerous wide-field surveys for transiting planets are underway, which we hope will provide a bounty of additional targets in the near future.

We acknowledge helpful discussions with T. Brown, E. Chiang, S. Gaudi, D. Lin, and G. Torres. We are grateful to J. Wisdom for advice on calculating the rate of tidal heating. Work by J.N.W. was supported by NASA through Hubble Fellowship grant HST-HF-01180.02-A, awarded by the Space Telescope Science Institute, which is operated by the Association of Universities for Research in Astronomy, Inc., for NASA, under contract NAS 5-26555. The visit of E.L.T. to the University of Tokyo was supported by an invitation fellowship program for research in Japan from the Japan Society for Promotion of Science (JSPS). This work was partly supported by a Grant-in-Aid for Scientific Research from JSPS grants 14102004 and 16340053, and by NASA grant NAG5-13148.

REFERENCES

- Alonso, R., et al. 2004, *ApJ*, 613, L153
- Baliunas, S. L., Henry, G. W., Donahue, R. A., Fekel, F. C., & Soon, W. H. 1997, *ApJ*, 474, L119
- Beck, J. G. 2000, *Sol. Phys.*, 191, 47
- Beck, J. G., & Giles, P. 2005, *ApJ*, 621, L153
- Beckers, J. M., & Nelson, G. D. 1978, *Sol. Phys.*, 58, 243
- Bodenheimer, P., Lin, D. N. C., & Mardling, R. A. 2001, *ApJ*, 548, 466
- Brown, T. M., Charbonneau, D., Gilliland, R. L., Noyes, R. W., & Burrows, A. 2001, *ApJ*, 552, 699
- Bundy, K. A., & Marcy, G. W. 2000, *PASP*, 112, 1421
- Butler, R. P., Marcy, G. W., Williams, E., McCarthy, C., Dosanji, P., & Vogt, S. S. 1996, *PASP*, 108, 500
- Charbonneau, D., Brown, T. M., Latham, D. W., & Mayor, M. 2000, *ApJ*, 529, L45

- Charbonneau, D., Brown, T. M., Gilliland, R. L., & Noyes, R. W. 2003, IAU Symposium, 219, electronic version available at: http://cfa-www.harvard.edu/~dcharbon/iau219_hd209458.pdf
- Cody, A. M., & Sasselov, D. D. 2002, *ApJ*, 569, 451
- Deming, D. et al. 2005, preprint
- Fischer, D. & Valenti, J. 2005, preprint
- Francois, P., Spite, M., Gillet, D., Gonzalez, J.-F., & Spite, F. 1996, *A&A*, 310, L13
- Gonzalez, G. 1998, *A&A*, 334, 221
- Greenberg, R. 1974, *Icarus*, 23, 51
- Hale, A. 1994, *AJ*, 107, 306
- Hale, A. 1995, *PASP*, 107, 22
- Henry, G. W., Marcy, G. W., Butler, R. P., & Vogt, S. S. 2000, *ApJ*, 529, L41
- Hosokawa, Y. 1953, *PASJ*, 5, 88
- Hut, P. 1980, *A&A*, 92, 167
- Hut, P. 1981, *A&A*, 99, 126
- Kant, I. 1755, *General History of Nature and Theory of the Heavens* (Königsberg: Petersen)
- Kopal, Z. 1980, *Ap&SS*, 70, 329
- Kurucz, R. L., Furenlid, I., & Brault, J. T. L. 1984, *National Solar Observatory Atlas, Sunspot*, New Mexico: National Solar Observatory, 1984
- Laplace, P. S. 1796, *Exposition du système du monde* (Paris: Cercle-Social)
- Laughlin, G. et al. 2005, *ApJ*, 629, L121
- Mandel, K., & Agol, E. 2002, *ApJ*, 580, L171
- Mazeh, T., et al. 2000, *ApJ*, 532, L55
- McLaughlin, D. B. 1924, *ApJ*, 60, 22
- Miralda-Escudé, J. 2002, *ApJ*, 564, 1019
- Ohta, Y., Taruya, A., & Suto, Y. 2005, *ApJ*, 622, 1118 [OTS]
- Peale, S. J. & Cassen, P. 1978, *Icarus*, 36, 245
- Press, W. H., Teukolsky, S. A., Vetterling, W. T., & Flannery, B. P. 1992, *Numerical Recipes in C* (Cambridge University Press), pp. 408, 689
- Queloz, D., Eggenberger, A., Mayor, M., Perrier, C., Beuzit, J. L., Naef, D., Sivan, J. P., & Udry, S. 2000, *A&A*, 359, L13
- Rasio, F. A., Tout, C. A., Lubow, S. H., & Livio, M. 1996, *ApJ*, 470, 1187

Rossiter, R. A. 1924, ApJ, 60, 15

Saar, S. H., Butler, R. P., & Marcy, G. W. 1998, ApJ, 498, L153

Snellen, I.A.G. 2004, MNRAS, 353, L1

Terquem, C., Papaloizou, J. C. B., Nelson, R. P., & Lin, D. N. C. 1998, ApJ, 502, 788

Winn, J. N. & Holman, M. J. 2005, ApJ, 628, L159

Wisdom, J. 2004, AJ, 128, 484

Table 1. Orbital, stellar, and planetary properties of HD 209458

Parameter	Best Fit (mean)	Uncertainty (σ)	Lower 90% Confidence Limit	Upper 90% Confidence Limit	Notes
M_p (M_{Jup})	0.657	0.006	0.647	0.668	1
M_p (M_{Jup})	0.657	...	0.594	0.721	2
R_* (R_\odot)	1.148	0.002	1.143	1.152	1,3
R_* (R_\odot)	1.15	...	1.09	1.20	2,3
R_p (R_{Jup})	1.355	0.002	1.350	1.358	1,3
R_p (R_{Jup})	1.35	...	1.29	1.41	2,3
R_p/R_*	0.12096	0.00025	0.12056	0.12141	
$e \cos \omega$	0.0014	0.0022	−0.0021	0.0049	
$e \sin \omega$	0.0141	0.0055	0.0037	0.0232	3
e	0.0147	0.0053	0.0057	0.0234	3
ω (deg)	84	11	56	99	3
γ (m s $^{-1}$)	1.11	0.63	0.08	2.12	
Δt_1 (sec)	−5.7	2.0	−9.0	−2.6	
I (deg)	86.55	0.03	86.49	86.61	3
$v \sin I_*$ (km s $^{-1}$)	4.70	0.16	4.44	4.97	
λ (deg)	−4.4	1.4	−6.8	−2.1	
$v_1 \equiv u_2 + \frac{5}{3}u_1$	0.825	0.010	0.808	0.842	3
$v_2 \equiv u_2 - \frac{3}{5}u_1$	0.181	0.074	0.058	0.289	3

¹Based on the assumption $M_*/M_\odot = 1.06$.

²Incorporates the uncertainty in the stellar mass. The lower confidence limit is for $M_*/M_\odot = 0.93$, and the upper confidence limit is for $M_*/M_\odot = 1.19$.

³Depends on our particular choice of limb-darkening law. In reality, e is probably consistent with zero (see § 4.4).